

Spatial dependence of local density of states in semiconductor-superconductor hybrids

Qingzhen Wang,¹ Yining Zhang,¹ Saurabh Karwal,² and Srijit Goswami^{1,*}

¹*QuTech and Kavli Institute of Nanoscience, Delft University of Technology, Delft, 2600 GA, The Netherlands*

²*QuTech and Netherlands Organization for Applied Scientific Research (TNO), Delft, 2628 CK, The Netherlands*

Majorana bound states are expected to appear in one-dimensional semiconductor-superconductor hybrid systems, provided they are homogenous enough to host a global topological phase. In order to experimentally investigate the uniformity of the system, we study the spatial dependence of the local density of states in multiprobe devices where several local tunnelling probes are positioned along a gate-defined wire in a two-dimensional electron gas. Spectroscopy at each probe reveals a hard induced gap, and an absence of subgap states at zero magnetic field. However, subgap states emerging at finite magnetic field are not always correlated between different probes. Moreover, we find that the extracted critical field and effective g -factor of the lowest energy subgap state varies significantly across the length of the wire. Upon studying several such devices we do however find examples of striking correlations in the local density of states measured at different tunnel probes. We discuss possible sources of variations across devices.

INTRODUCTION

Majorana bound states (MBSs) obey non-Abelian exchange statistics and are potential building blocks of topological qubits [1, 2]. In this context, one-dimensional (1D) semiconductor-superconductor hybrids have been widely studied, where a topological phase transition is accompanied by the emergence of MBSs at the system edges [3, 4]. together with a closing and reopening of the superconducting gap in the hybrid bulk [5]. Tunnelling spectroscopy provides information about the local density of states (LDOS), and is often used to search for signatures of MBS [6]. However, it has been suggested that some of these observations could arise due to trivial reasons such as disorder or inhomogeneity of the chemical potential [7, 8]. Strong local perturbations would effectively segment the wire and thus prevent the creation of a global topological phase. It has therefore become clear that a prerequisite for reliably creating MBSs is spatial uniformity of microscopic properties across the length of the 1D hybrid system. These include the chemical potential, the induced superconducting gap and the effective g -factor.

Information about the bulk density of states of the hybrid region can be inferred by measuring the non-local conductance in a three-terminal geometry [9–11]. However, these measurements are only sensitive to the minimum energy scale of all the bulk states, and thus do not immediately reveal local properties. An alternative method to probe the bulk, and therefore get information about the wave function of subgap states, is to perform local tunnelling spectroscopy along the hybrid. While such experiments have been performed in hybrid nanowires, technical difficulties have led to soft superconducting gaps [12] or additional tunnelling currents that obscure the direct measurement of the LDOS in the hybrid [13]. Furthermore, the transparency of these tunnel probes is not tunable, thus preventing a systematic study of LDOS in the bulk. These issues can be mitigated by

using a two-dimensional electron gas (2DEG), which offers flexibility in device design and fabrication, allowing one to pattern an arbitrary number of tunable tunnel probes along the 1D hybrid, thus providing information about spatial variation in the LDOS. It has also been proposed that a gate-defined hybrid wire with multiple tunnel junctions is more resilient to inhomogeneous confinement potential, thereby making this device geometry a promising way to probe the LDOS [14].

Here we study the LDOS of quasi-1D hybrid wires, defined by electrostatic gating in an InSbAs 2DEG with epitaxial aluminium. Several tunnel probes positioned along the wire enables a simultaneous measurement of the position-dependent LDOS. At zero magnetic field, we measure a hard superconducting gap without any subgap states, confirming a strong proximity effect and the presence of clean tunnel junctions. As we increase the magnetic field, we in general do not observe any obvious correlation between the emerging subgap states at neighbouring probes, suggesting that these states are localized within 250 nm along the hybrid. Furthermore, we find that the critical field (B_c) and the effective g -factor (g^*) exhibit significant fluctuations along the wire. In contrast, some devices show remarkably correlated subgap states with a spatial extension of more than 1.1 μm . We discuss possible explanations of this inconsistency between different devices.

RESULTS

Device and basic characterization

The InSbAs 2DEG with epitaxial aluminium grown by molecular beam epitaxy has been shown to have a good proximity effect, high g -factor and large spin-orbit coupling [15, 16]. The structure of the multiprobe devices is illustrated in Fig. 1, together with the circuit diagram. First a 2.5 μm -long, 130 nm-wide aluminium

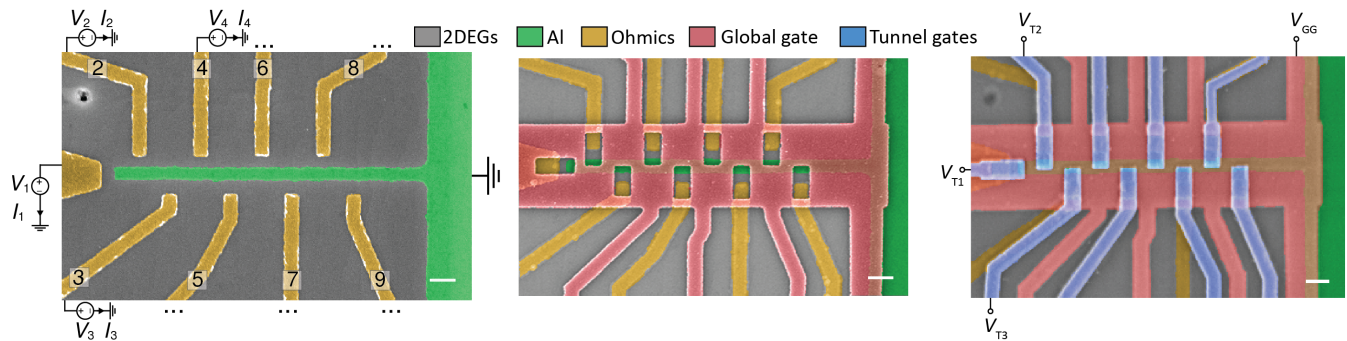


FIG. 1. **The multiprobe device.** (a) A false-colored scanning electron microscope (SEM) image of a device with the Al strip and normal contacts. Nine normal contacts are placed from the edge of the wire (“1”) to the bulk (up till “9”). In the circuit diagram, the applied bias voltages and measured currents are only shown for the first four probes for simplicity. (b) SEM image of a device after the global gate deposition. (c) SEM image of a device after the tunnel gates deposition. The applied global gate voltages V_{GG} and the applied voltages of the first four tunnel gates V_{T1} to V_{T4} are labelled. The first and second images are from lithographically similar devices. All scale bars here are 200 nm.

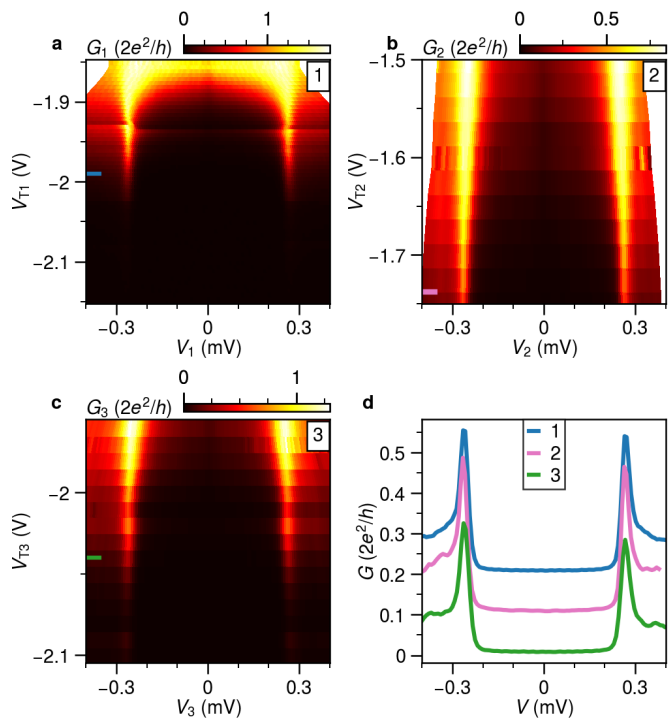


FIG. 2. **Hard superconducting gap at zero magnetic field.** (a) Tunnelling conductance G_i as a function of individual tunnel gate TG_i and the corresponding applied bias voltage V_i ($i \in \{1, 2, 3\}$). With a substantial change of the out-of-gap state conductance, no discrete subgap states are observed within the gap, indicating clean tunnel junctions. Probe numbers are labelled on the top-right corner. (b) Exemplary line traces indicate that the presence of two sharp coherence peaks and a hard induced superconducting gap (the lines are laterally offsetted by $0.1G_0$ for clarity). The measured lock-in signals are higher than the noise floor due to the additional parasitic capacitance in the circuit and a detailed comparison with the numerical derivative of the DC current is made in the Fig. S1. V_{GG} is at -2.6 V.

strip is defined by chemical etching and nine Ti/Pd normal contacts are deposited along the strip with a center-to-center separation of 250 nm. The aluminium strip remains electrically grounded during measurement, and the bias voltages applied on each contact V_i ($i \in \{1, 2, \dots, 9\}$) can be varied independently. After depositing a 20 nm thick AlOx dielectric layer, a global gate (GG) is deposited. Applying a negative voltage to GG depletes the 2DEG around the Al strip, thereby defining the 1D hybrid wire. At the same time, the 2DEGs between any two normal contacts are also depleted, ensuring that no current flows between neighboring tunnel probes. After depositing an additional 20 nm layer of AlOx, nine tunnel gates are deposited over the pinholes in the GG. The applied tunnel gate voltages V_{Ti} ($i \in \{1, 2, \dots, 9\}$) control the individual tunnel barrier, allowing one to perform local spectroscopy along the wire. The final image of one of the three measured devices (denoted Device A) is shown in Fig. 1c. We also present measurements of two other devices (denoted device B and C) with the same material but with only four tunnel probes (device images shown in Fig. 5).

All measurements were conducted in a dilution refrigerator with 20 mK base temperature with standard lock-in techniques. More details about the measurement scheme can be found in the measurements methods in the supplementary information.

We begin the device characterization through tunnelling spectroscopy measurements as a function of tunnel gates. Three examples of the measured spectrum are illustrated in Fig. 2(a-c). In the tunnelling regime (Fig. 2d), all three probes show sharp superconducting coherence peaks at approximately ± 0.26 meV and a suppression of the in-gap conductance. The tunnel gate voltages V_{Ti} affect the transparency of the tunnel junctions. While the the out-of-gap conductance varies between around half of the G_0 to nearly zero, the co-

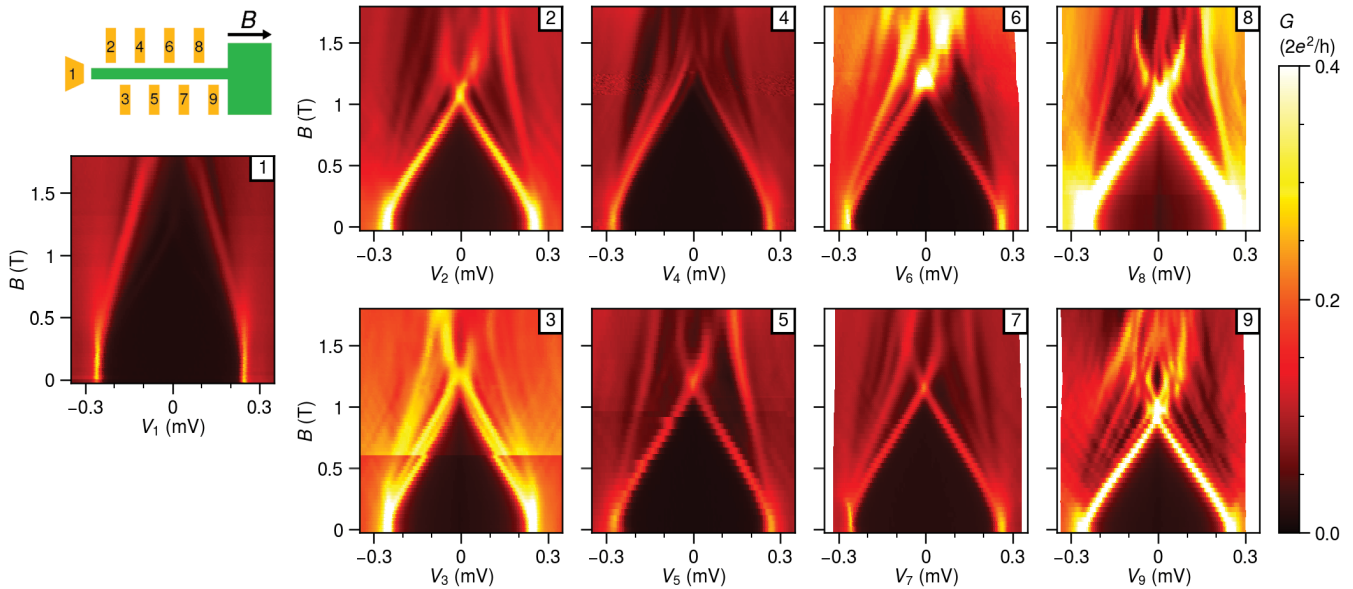


FIG. 3. **Field evolution of LDOS for device A.** Tunneling conductance G of each tunnel probes with a schematic of the device. The measurements of probe 1234 and 6789 are obtained by sweeping the four biases at the same time and recording the signals with four lock-in amplifiers. The spectrum of probe 5 is obtained in a three-terminal measurement circuit. No obvious correlation of subgap states between neighboring probes are observed. V_{GG} is at -2.6 V.

herence peaks remain at the same energies, as shown in Fig. 2a-c. Importantly, we note that there are no obvious charging effects, and no additional subgap states appear over this range of transparency. These spurious states are often observed in hybrid devices and are attributed to a nonuniform confinement potential in the semiconductor junctions [14, 17, 18]. The absence of these subgap states at zero magnetic field allows us to extract information about the LDOS in the hybrid wire.

Spatial dependence of microscopic parameters

The precursor of MBSs in a 1D hybrid system is an extended Andreev bound state (ABS) across the entire wire. By applying a large enough magnetic field, a topological phase may arise, where the ABS evolves into spatially separated MBSs localized at the ends of the wire. A persisting ZBP is then expected to appear at the edges, along with a closing and reopening of the gap in the bulk of the wire. If the spatial separation of a series of tunnel probes is sufficiently small, it should then be possible to map the wave function of the MBSs, which in theory decays exponentially from the wire edge into the bulk [14].

We measure the tunnelling conductance as a function of the individual applied bias V_i and a global magnetic field B parallel to the aluminium strip, as shown in Fig. 3. The tunnel gates voltages are adjusted such that

all probes have out-of-gap conductance well below G_0 , and are therefore in the tunnelling regime. The most clear observation from Fig. 3 is that there is no systematic correlation in the field evolution of the subgap states moving from the edge to the bulk, indicating the absence of an extended ABS in the wire. For example, the field value where the lowest subgap states cross zero energy differs by about 400 mT between probe 1 and 9. Furthermore, even when we compare the subgap states from neighboring probes (separated by 250 nm), their evolution with magnetic field seems uncorrelated. For example, the subgap states from probe 2 reach zero energy at around 1.1 T while this occurs at 1.3 T for probe 3. The measured spectra of probe 3, 5 and 7 look qualitatively similar, but a more detailed comparison shows that the extracted microscopic parameters are different, and thus these subgap states are also not actually correlated (detailed in Fig. 4). The measured tunnel spectra at individual probes can also depend on the chemical potential in the wire. Thus we also performed the measurements at $V_{GG} = -1.8$ V, just below the threshold voltage required to deplete the bare 2DEG. Similarly uncorrelated subgap states are observed for this set of measurements (Fig. S2).

We use the the measurement presented in Fig. 3 and Fig. S2 to extract the spatial dependence of three microscopic parameters in the hybrid: the induced superconducting gap Δ , the critical field B_c and the effective g -factor g^* of the lowest-energy subgap states.

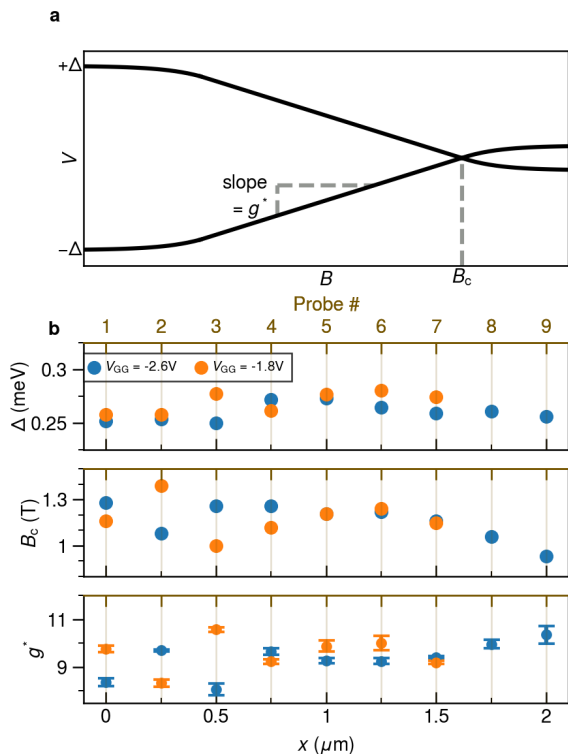


FIG. 4. **Spatial dependence of superconducting gap Δ , critical field B_c and effective g^* .** (a) A sketch of the field dependence of the lowest subgap states. (b) Δ , B_c and g^* are plotted as a function of distance x to the edge of the wire (bottom axis) and the corresponding probe number (top axis).

They are labelled in an exemplar field evolution of the lowest subgap states, as shown in Fig. 4a. The size of the induced gap Δ , B_c and g^* characterize the degree of hybridization of the wavefunction across the superconductor-semiconductor interface. It has been shown that this coupling between the two materials in hybrid nanowires can be modulated by the use of the electric field [10, 19, 20]. Δ is determined by locating the applied bias voltages corresponding to the coherence peaks maxima at $B = 0$. B_c is defined here as the field value at which the lowest states reach zero energy and is extracted by locating the first local maximum in the zero-bias conductance traces as a function of magnetic field. g^* is defined by $g_{eff} = \frac{2}{\mu_B} \left| \frac{\Delta E}{\Delta B} \right|$ [21], where μ_B is Bohr magneton and $\left| \frac{\Delta E}{\Delta B} \right|$ the absolute average of the slope from the linear fitting of the lowest subgap states at positive and negative biases.

As seen in Fig. 4b, the induced gap Δ in our devices varies between 0.25 meV and 0.28 meV along the wire, with an average value of 0.26 mV ($GG = -2.6V$) and 0.27 mV ($GG = -1.8V$). Additionally, the similar magnitude at two different V_{GG} is probably due to the weak gating effect of the hybrid sections, which is achieved

purely by the fringing field of the applied global gate voltages. The spread of the data points can be captured by the calculated coefficient of variation (CV), which is the ratio of the standard deviation to the mean. CV_Δ about 3.1% for $GG = -2.6V$ and 3.4% for $GG = -1.8V$. This variation may be due to mesoscopic variations in the wire or the different tunnel broadening at each probe. For the critical field B_c , however, we find a much stronger variation of the extracted values across different probes. The averaged value is at 1.16 T for $GG = -2.6V$ and 1.18 T for $GG = -1.8V$, with the CV reaching about 9.4% in both cases. This significant spread could arise from a nonuniform electro-chemical potential in the wire, which is undesirable in realizing a global topological phase transition. The effective g -factor is indicative of the extent of hybridization of wavefunction throughout the cross-sectional interface of the hybrid [19–21], and eventually determines the required critical field for a topological phase transition. The extracted data here shows a large amount of fluctuation, ranging from about 8 to 11. These values are significantly smaller than the g -factor of bare InSbAs 2DEGs [15, 22], indicative of hybridization with the superconductor. The error bars originate from the process of linear fitting. For $V_{GG} = -2.6V$, the mean is 9.4 with a CV of 6.7%, and for $V_{GG} = 1.8V$, the mean is 9.6 with a CV of 7.5%. The significant spread of B_c and g^* , together with the uncorrelated LDOS shown in Fig. 3, indicates a non-uniform chemical potential along the wire, which is nonideal for creating Majoranas.

Extended subgap states in other multiprobe devices

We repeat similar measurements in two additional multiprobe devices with a similar design. The SEM images of devices B and C are shown in Fig. 5a and Fig. 5c, respectively. These devices are fabricated with the same 2DEG heterostructures and have the identical shape of Al strip. However, four normal probes are now arranged with a larger separation of around 500 nm. Basic characterization in Fig. S4 confirms similar hard gap and absence of subgap states in tunnelling spectroscopy, as the behaviour observed in device A. Field dependence measurements are conducted in a comparable tunnelling regime as depicted in Fig. 3 for the first three probes from the edge for both devices. Remarkably, the subgap states of probe 1 and probe 3 now have a remarkably similar dependence on the magnetic field, which we attribute to extended states over 1.1 μm . However, spectroscopy at probe 2 looks different. While some states evolve similarly at all three probes (Fig. S6), others do not. This suggests that the wavefunction of these states is not uniform across the width of the hybrid region. The measurements for device C shows that the lowest subgap states from all probes have the same dependence on the magnetic field, confirming their spatial correlation over

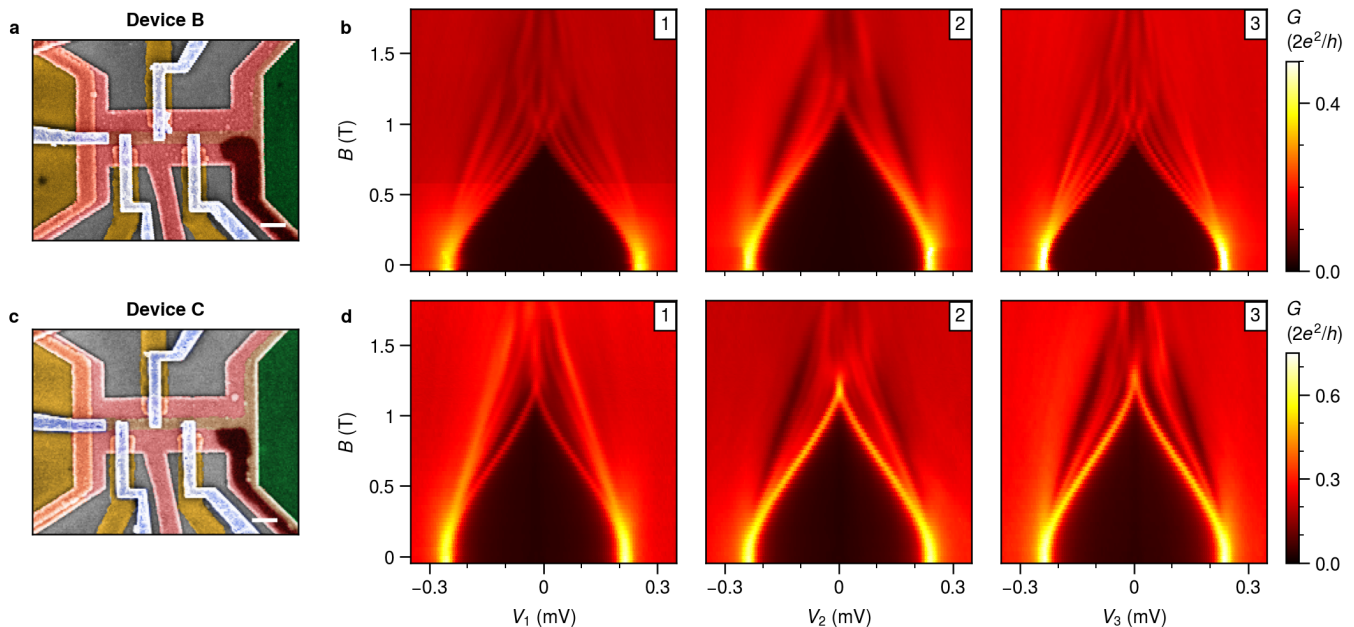


FIG. 5. **Field evolution of LDOS on device B and C.** (a) The false-colored SEM image of device B with a similar shape of Al strip, but only four normal contacts that are separated by around 500 nm. The scale bar here is 200 nm. (b) The field dependence of the leftmost three tunnel probes. The lowest three subgap states spectra have almost the same field dependence between probe 1 and probe 3, but only the second lowest subgap states are present in probe 2. (c) The false-colored SEM image of another four-probe device C and (d) the field evolution. The lowest subgap states are almost perfectly correlated within all three probes. Details on peak-matching for confirming these correlations are shown in Fig. S6.)

1.1 μm (Fig. S6).

DISCUSSION

The variations in the extent of the ABS wavefunction across different devices warrants a further discussion. We propose a few explanations for this observed discrepancy. First of all, we know that the semiconductor 2DEGs used in this study have a typical peak mobility of about $28\,000\text{ cm}^2/\text{Vs}$ (which corresponds to a mean-free path of about 280 nm) [15]. Thus, intrinsic disorder could be a factor responsible for the device to device variations. Secondly, the system could be sensitive to potential inhomogeneities arising from electrostatic gating. The tuning of chemical potential of a 1D hybrid wire is determined in part by the fringing field of the global gate. The roughness in the edge profile of the aluminium could therefore result in local variations of chemical potential along the wire. This may explain the observations in device B (Fig. 5b) where the spectra are only correlated on one side of the wire.

Additionally, while the device geometry of device A looks nominally similar to that of device B/C (apart from the number of probes), they actually have different dimensions of the pinholes and dielectric thicknesses (Fig. S5), which could potentially lead to different electric fields at the hybrid region. In fact, we ob-

serve this experimentally while measuring the tunnelling spectra as a function of tunnel gate voltages at finite field (Fig. S4). The lowest energy subgap states in device A can be affected upon changing the the corresponding tunnel gate voltages, in contrast with device B/C, where they remain unaffected. To qualitatively understand this difference, we performed electrostatic simulations in COMSOL, based on the realistic device geometry (Fig. S5). We find that in device A, the tunnel gate voltages can create stronger fringing fields in the hybrid region (Fig. S3) and thereby effectively lead to the formation of invasive tunnel probes. On the other hand, as a result of the narrower pinholes and the thicker dielectric layers, the tunnel gates in device B/C have a significantly weaker effect on the hybrid region. This is in accordance with the experimental observations whereby device B/C show stronger correlations between probes as compared to device A. Therefore, it is important to take these electrostatic effects into consideration while designing devices to study the LDOS in hybrid systems.

CONCLUSIONS

In conclusion, we have used tunnelling spectroscopy to investigate the local density of states in gate-defined wires based on a 2DEG semiconductor-superconductor hybrid structure. This is achieved by implementing a

multiprobe device geometry, with up to nine side probes placed at different positions along the wire. At zero magnetic field, we observed hard superconducting gaps and clean tunnel junctions, indicating uniform proximity over $2.5\ \mu\text{m}$. As the magnetic field increases, subgap states appear and eventually cross zero energy. However, these states are generally not correlated between neighboring probes. The critical field B_c and effective g -factor g^* are extracted at two different global gate voltages V_{GG} and exhibit significant spatial fluctuations. Measurements from comparable devices show a completely different behaviour, where the subgap states evolve identically as a function of magnetic field, suggesting correlations over $1.1\ \mu\text{m}$. In particular, even in the case of perfect probe-to-probe correlation, we find no clear evidence of a gap reopening, suggesting that the non-uniformity in our devices may be more than what is required to host a global topological phase [23].

REFERENCE

* s.goswami@tudelft.nl

- [1] A. Y. Kitaev, Unpaired Majorana fermions in quantum wires, *Physics-Uspekhi* **44**, 131 (2001).
- [2] C. Nayak, S. H. Simon, A. Stern, M. Freedman, and S. Das Sarma, Non-Abelian anyons and topological quantum computation, *Rev. Mod. Phys.* **80**, 1083 (2008).
- [3] R. M. Lutchyn, J. D. Sau, and S. Das Sarma, Majorana fermions and a topological phase transition in semiconductor-superconductor heterostructures, *Phys. Rev. Lett.* **105**, 077001 (2010).
- [4] Y. Oreg, G. Refael, and F. von Oppen, Helical liquids and Majorana bound states in quantum wires, *Phys. Rev. Lett.* **105**, 177002 (2010).
- [5] T. D. Stanescu, S. Tewari, J. D. Sau, and S. Das Sarma, To close or not to close: The fate of the superconducting gap across the topological quantum phase transition in Majorana-carrying semiconductor nanowires, *Phys. Rev. Lett.* **109**, 266402 (2012).
- [6] R. M. Lutchyn, E. P. A. M. Bakkers, L. P. Kouwenhoven, P. Krogstrup, C. M. Marcus, and Y. Oreg, Majorana zero modes in superconductor-semiconductor heterostructures, *Nature Reviews Materials* **3**, 52 (2018).
- [7] H. Pan and S. Das Sarma, Physical mechanisms for zero-bias conductance peaks in Majorana nanowires, *Phys. Rev. Res.* **2**, 013377 (2020).
- [8] R. Hess, H. F. Legg, D. Loss, and J. Klinovaja, Trivial Andreev band mimicking topological bulk gap reopening in the nonlocal conductance of long Rashba nanowires, *Phys. Rev. Lett.* **130**, 207001 (2023).
- [9] T. O. Rosdahl, A. Vuik, M. Kjaergaard, and A. R. Akhmerov, Andreev rectifier: A nonlocal conductance signature of topological phase transitions, *Phys. Rev. B* **97**, 045421 (2018).
- [10] N. van Loo, G. P. Mazur, T. Dvir, G. Wang, R. C. Dekker, J.-Y. Wang, M. Lemang, C. Sfiligoj, A. Bordin, D. van Driel, G. Badawy, S. Gazibegovic, E. P. A. M. Bakkers, and L. P. Kouwenhoven, Electrostatic control of the proximity effect in the bulk of semiconductor-superconductor hybrids, *Nature Communications* **14**, 3325 (2023).
- [11] M. Aghaee, A. Akkala, Z. Alam, R. Ali, A. Alcaraz Ramirez, M. Andrzejczuk, A. E. Antipov, P. Aseev, M. Astafev, B. Bauer, J. Becker, S. Boddapati, *et al.* (Microsoft Quantum), InAs-Al hybrid devices passing the topological gap protocol, *Phys. Rev. B* **107**, 245423 (2023).
- [12] A. Grivnin, E. Bor, M. Heiblum, Y. Oreg, and H. Shtrikman, Concomitant opening of a bulk-gap with an emerging possible Majorana zero mode, *Nature Communications* **10**, 1940 (2019).
- [13] V. Levajac, J.-Y. Wang, C. Sfiligoj, M. Lemang, J. C. Wolff, A. Bordin, G. Badawy, S. Gazibegovic, E. P. A. M. Bakkers, and L. P. Kouwenhoven, Subgap spectroscopy along hybrid nanowires by nm-thick tunnel barriers, *Nature Communications* **14**, 6647 (2023).
- [14] T. D. Stanescu and S. Das Sarma, Building topological quantum circuits: Majorana nanowire junctions, *Phys. Rev. B* **97**, 045410 (2018).
- [15] C. M. Möhle, C. T. Ke, Q. Wang, C. Thomas, D. Xiao, S. Karwal, M. Lodari, V. V. D. Kerkhof, R. Termaat, G. C. Gardner, G. Scappucci, M. J. Manfra, and S. Goswami, InSbAs two-dimensional electron gases as a platform for topological superconductivity, *Nano Lett.* **21**, 9990 (2021).
- [16] S. Metti, C. Thomas, D. Xiao, and M. J. Manfra, Spin-orbit coupling and electron scattering in high-quality InSb_{1-x}As_x quantum wells, *Phys. Rev. B* **106**, 165304 (2022).
- [17] E. Prada, P. San-Jose, and R. Aguado, Transport spectroscopy of ns nanowire junctions with Majorana fermions, *Phys. Rev. B* **86**, 180503 (2012).
- [18] M. Valentini, F. Peñaranda, A. Hofmann, M. Brauns, R. Hauschild, P. Krogstrup, P. San-Jose, E. Prada, R. Aguado, and G. Katsaros, Nontopological zero-bias peaks in full-shell nanowires induced by flux-tunable Andreev states, *Science* **373**, 82 (2021).
- [19] M. W. A. de Moor, J. D. S. Bommer, D. Xu, G. W. Winkler, A. E. Antipov, A. Bargerbos, G. Wang, N. van Loo, R. L. M. O. het Veld, S. Gazibegovic, D. Car, J. A. Logan, M. Pendharkar, J. S. Lee, E. P. A. M. Bakkers, C. J. Palmstrøm, R. M. Lutchyn, L. P. Kouwenhoven, and H. Zhang, Electric field tunable superconductor-semiconductor coupling in Majorana nanowires, *New Journal of Physics* **20**, 103049 (2018).
- [20] J.-Y. Wang, N. van Loo, G. P. Mazur, V. Levajac, F. K. Malinowski, M. Lemang, F. Borsoi, G. Badawy, S. Gazibegovic, E. P. A. M. Bakkers, M. Quintero-Pérez, S. Heedt, and L. P. Kouwenhoven, Parametric exploration of zero-energy modes in three-terminal insb-al nanowire devices, *Phys. Rev. B* **106**, 075306 (2022).
- [21] S. Vaitiekėnas, M.-T. Deng, J. Nygård, P. Krogstrup, and C. M. Marcus, Effective g factor of subgap states in hybrid nanowires, *Phys. Rev. Lett.* **121**, 037703 (2018).
- [22] S. Metti, C. Thomas, and M. J. Manfra, Electronic g factor and tunable spin-orbit coupling in a gate-defined InSbAs quantum dot, *Phys. Rev. B* **108**, 235306 (2023).

- [23] S. Ahn, H. Pan, B. Woods, T. D. Stanescu, and S. Das Sarma, Estimating disorder and its adverse effects in semiconductor Majorana nanowires, *Phys. Rev. Mater.* **5**, 124602 (2021).
- [24] E. A. Martinez, A. Pöschl, E. B. Hansen, M. A. Y. van de Poll, S. Vaitiekėnas, A. P. Higginbotham, and L. Casparis, Measurement circuit effects in three-terminal electrical transport measurements, arXiv:2104.02671 (2021).

ACKNOWLEDGMENTS

We would like to express our gratitude to Nick van Loo and Greg Mazur for their constant support and productive, in-depth discussions at various stages of the work. We also want to thank Ji-Yin Wang, Vukan Levajac, Bas ten Haaf and Christian Prosko for providing valuable feedback on the manuscript. We thank Di Xiao, Candice Thomas and Michael J. Manfra for providing the semiconductor heterostructures used in this work. The experimental research at Delft was supported by the Dutch National Science Foundation (NWO) and a TKI grant of the Dutch Topsectoren Program.

AUTHOR CONTRIBUTIONS

Q.W. and S.K. fabricated the devices. Measurements were performed by Y.Z. and Q.W. The manuscript was written by Q.W., Y.Z. and S.G., with inputs from all coauthors. S.G. supervised the experimental work.

DATA AVAILABILITY

Raw data and analysis scripts for all presented figures are available at zenodo.org/doi/10.5281/zenodo.11203149

SUPPLEMENTARY INFORMATION

FABRICATION

Three devices were measured to obtain the data presented in the main text and Supplementary (device A, B and C). To prevent the potential intermixing of Al and Sb at high temperature, all the fabrication processes are performed at room temperature unless otherwise specified. We use electron beam lithography to define the required nano-structures and use unexposed PMMA as etch masks. The device fabrication starts by etching the Al and the 2DEG in undesired areas. The Al etch is performed in Transene D etchant at a temperature of 48.2 °C for 9 s. Afterwards, using the same PMMA mask, the 2DEG is etched in a III-V etchant (560 mL deionized water, 5 mL H₂O₂ and 4 mL 85% H₃PO₄ and 9.6 g citric acid powder) for 70 s. This leads to an etching depth of about 75 nm and produces a series of un-etched units (called "mesa") which are electrically isolated. Then a set of fine markers made of Ti/Au are evaporated around each mesa. The purpose of the fine markers is to improve the alignment accuracy between the Al strip, normal contacts and two gate layers to ensure the functionality of the final device. The next step is to define the Al strip, where we carry out a second Al etch in 38.2 °C Transene D for 10 s. Multiple fine normal contacts made of 5 nm/15 nm Ti/Pd are then deposited around the Al strip. Subsequently, a thicker 5 nm/115 nm Ti/Au evaporation defines the contact leads. Afterwards, we deposit a 20 nm-thick global AlO_x dielectric at 40 °C. The first layer of gate electrodes (global gate) are formed with a 5 nm/25 nm Ti/Pd evaporation for the fine structures, and then a 5 nm Ti and 115 nm Au evaporation for the coarse gate leads. After depositing the second layer of 20 nm-thick global AlO_x dielectric, we deposit a 5 nm/35 nm Ti/Au for the fine structure of the second gate layer and an additional 5 nm Ti/115 nm Ti/Au evaporation for the coarse gate leads.

MEASUREMENT METHODS

For all the measurements, the alignment of the magnetic field with respect to the gate-define wire is expected to be accurate within $\pm 10^\circ$ and calibrated through performing tunnelling spectroscopy of the hybrid section as a function of field angle. During the transport measurement, the aluminium is always electrically grounded. Each available Ohmic lead is biased with both DC and AC voltages and also connected to a current-to-voltage converter, transmitting the outcome to Keithley multimeter DM6500 and lock-in amplifier SR830. Two types of circuits are implemented: for the results presented in Fig. 2, probe 5 in Fig. 3 and Fig. 5b, a common three-terminal circuit as presented in [24] is used. The rest of

measurements, in Fig. 3 and Fig. 5d, are acquired with a special multi-terminal circuit. For the case of Fig. 3, the same DC voltage biases are applied on four different probes simultaneously, but each with an AC excitation of distinct frequencies. Thus, we can register four lock-in responses concurrently and perform more efficient measurements. In particular, we have compared the results obtained in the multi-terminal circuit configuration with those obtained with the simplistic two-terminal circuit, and found no qualitative difference in determining the energies of the subgap states Fig. S7.

In the three-terminal circuit, when a DC voltage and a lock-in AC excitation is applied to one Ohmic contact, the another one is kept grounded and vice versa. The amplitudes of AC excitations are always 5 μ V and frequencies are 19.99 Hz (lockin-1) and 29.99 Hz (lockin-2). In this way, we can measure the full conductance matrix G in two measurement runs. In the multi-terminal circuits, if two DC biases are swept simultaneously, the frequencies of the AC excitations are 19.99 Hz (lockin-1) and 27.77 Hz (lockin-2). If four DC biases are swept, the frequencies of the AC excitations are 23.33 Hz (lockin-1), 27.77 Hz (lockin-2), 13.33 Hz (lockin-3) and 19.99 Hz (lockin-4). Therefore, the tunnelling signals at each tunnel probe can only be demodulated by the single lock-in amplifier whose AC excitation has the same frequency. The voltage-divider effect is accounted for by correcting the real DC voltage drop on each contact with the known fridge line resistances and the resistance from the current-to-voltage converter module. In this way, the evolution of the energies of the subgap states as a function of gate voltage or magnetic field can be correctly resolved. Offsets of the applied voltage biases on each contacts are corrected via averaging the coherence peaks in the conductance line traces.

COMSOL SIMULATIONS

We use AC/DC module in COMSOL Multiphysics 6.1 to simulate the electrostatics in a simplified but realistic geometry. To be more precise, the following specifications are taken directly from the multiprobe devices shown in the main text: the thickness of the 2DEG, the width and thickness of the aluminium strip, the thickness of the AlO_x dielectric, the relative position and the size of the pinhole, the thickness of the global gate and tunnel gate layer. Note that the 2DEG is treated as a semiconductor material with a relative permittivity of 17.7. Aluminium is kept electrically ground and the voltages are applied to the global gate and the tunnel gate. The only variance between device A and device B/C are the different AlO_x thickness and the width of the pinhole. The plots shown in Fig. S5 are obtained by performing a parametric sweep of the V_{GG} and V_{TG} with 1 V step.

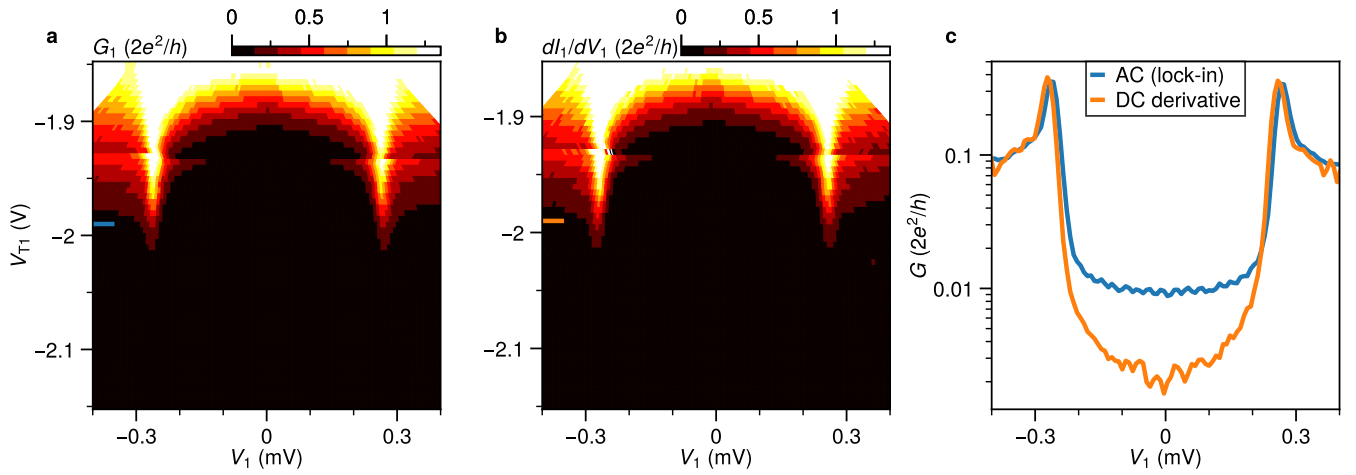


FIG. S1. **Comparison of the AC and DC signals** In this example, the conductance is either measured directly with lock-in amplifier (**a**, Figure 2a in the main text), or calculated with a numerical derivative of the DC current (**b**). The line-cut taken at the same gate voltage (**c**) shows that the in-gap conductance in the DC derivative is about an order of magnitude smaller than that of the lock-in signal. This is because the additional parasitic components in the circuit induce an additional phase shift, thus making the amplitude of the measured lock-in signal higher. A Savitzky–Golay filter of window length of 5 is applied for the DC current before taking the numerical derivation.

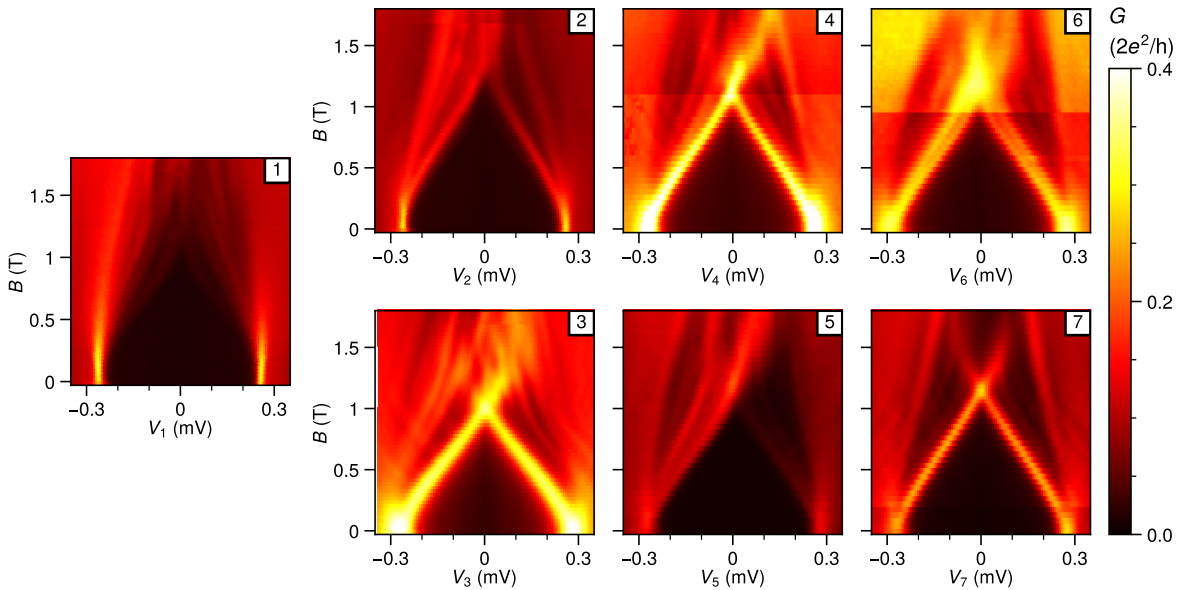


FIG. S2. **Field evolution of LDOS at $V_{GG} = -1.8$ V: Device A.** Similar to the behavior observed in main text FIG. 3, no obvious correlation of subgap states between neighboring probes are observed. Note that the field evolution has only been recorded for the first seven probes because of difficulties in adjusting the the tunnel gates for Probe 8 and Probe 9.

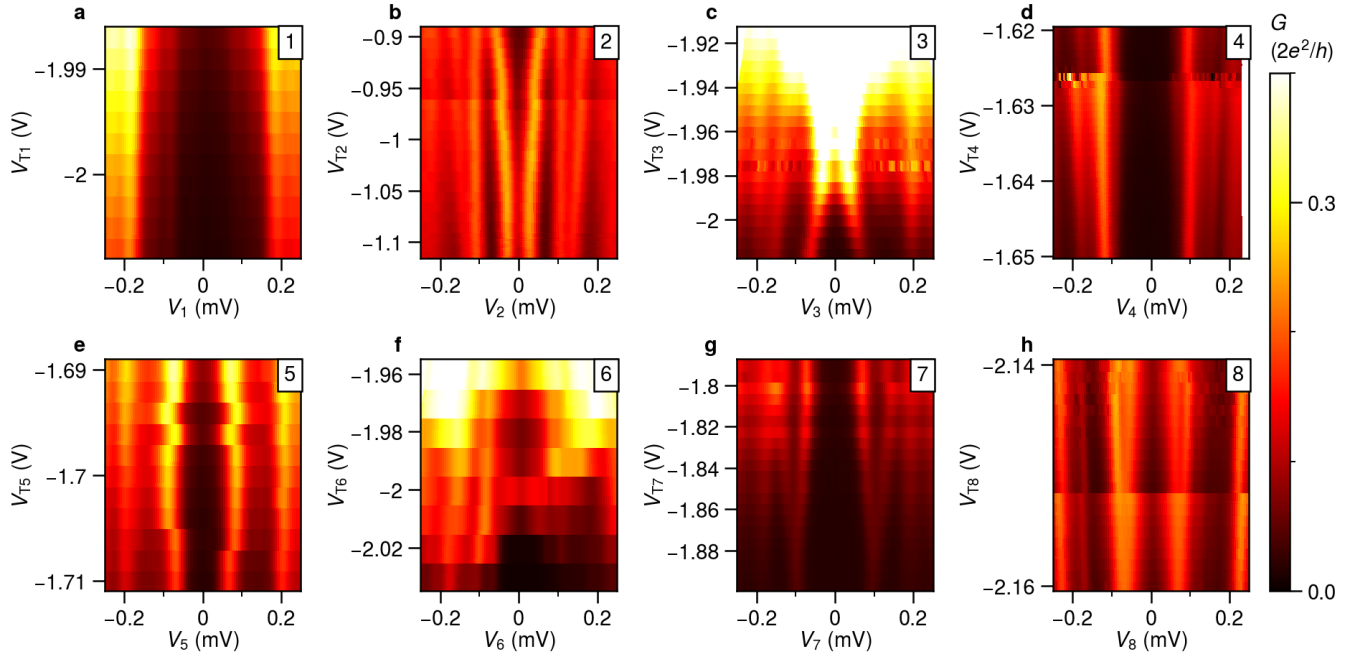


FIG. S3. **Effect of tunnel gates on spectroscopy: Device A.** The probe numbers are indicated in the top left of each figure. Overall, the subgap states do not stay at constant energies upon changing the corresponding tunnel gate voltages, indicating that the tunnel gates can have an effect on the hybrid region. This observation also indicates that the electrostatics can lead to false-positive observation of correlated subgap states, as a result of fine-tuned gate voltages.

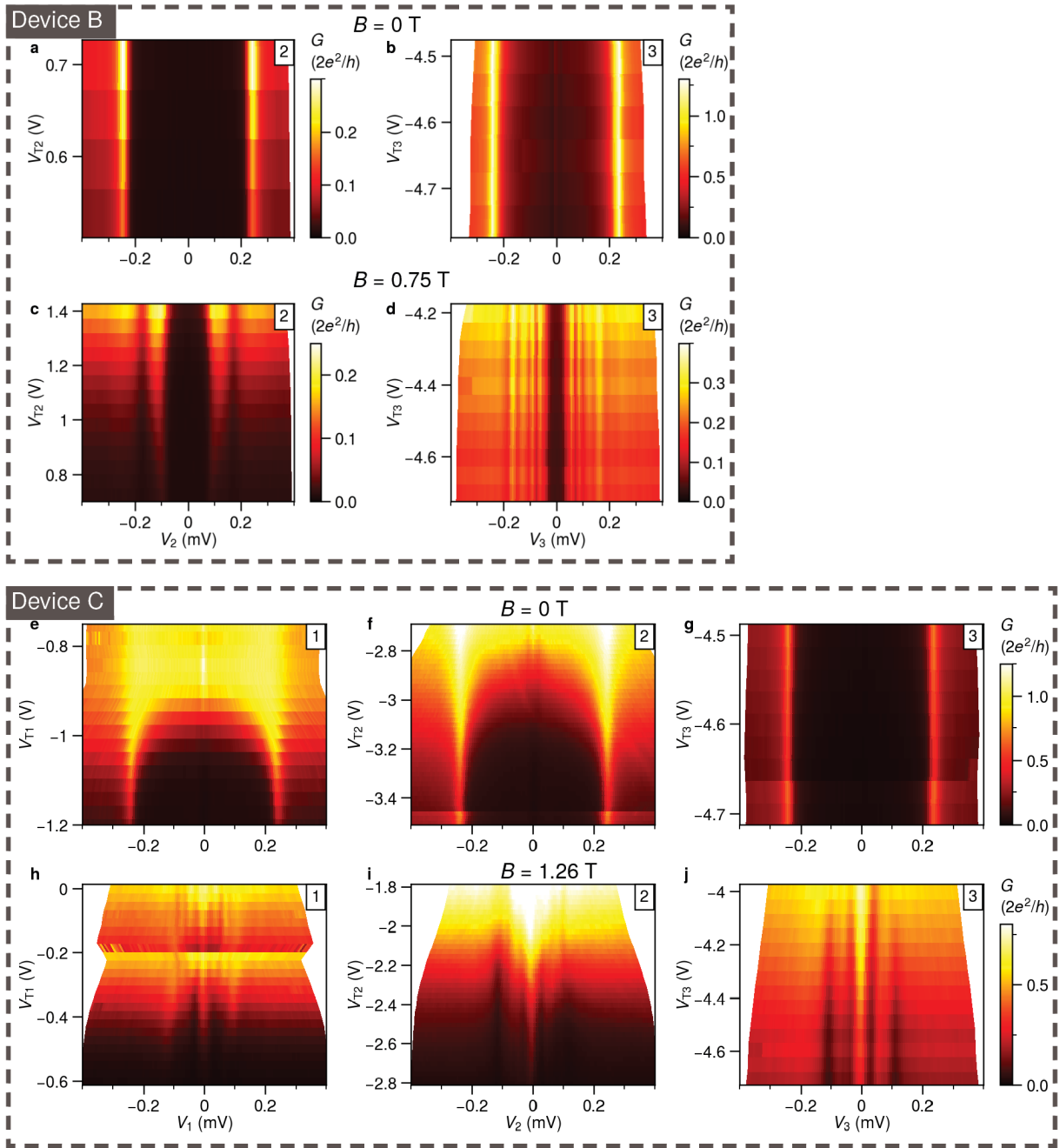


FIG. S4. **Effect of tunnel gates on spectroscopy: Device B and C.** Hard gaps without the subgap states ((a-b) and (e-g)) are observed for both devices. At a finite field, the subgap states stay at almost the same energies as a function of tunnel gate voltages over a large range of transparency ((c-d) and (h-j)). Note that for device B, the tunnel gate T1 has almost no tunability of the junction transparency, and therefore only the T2 and T3-dependence are shown here.

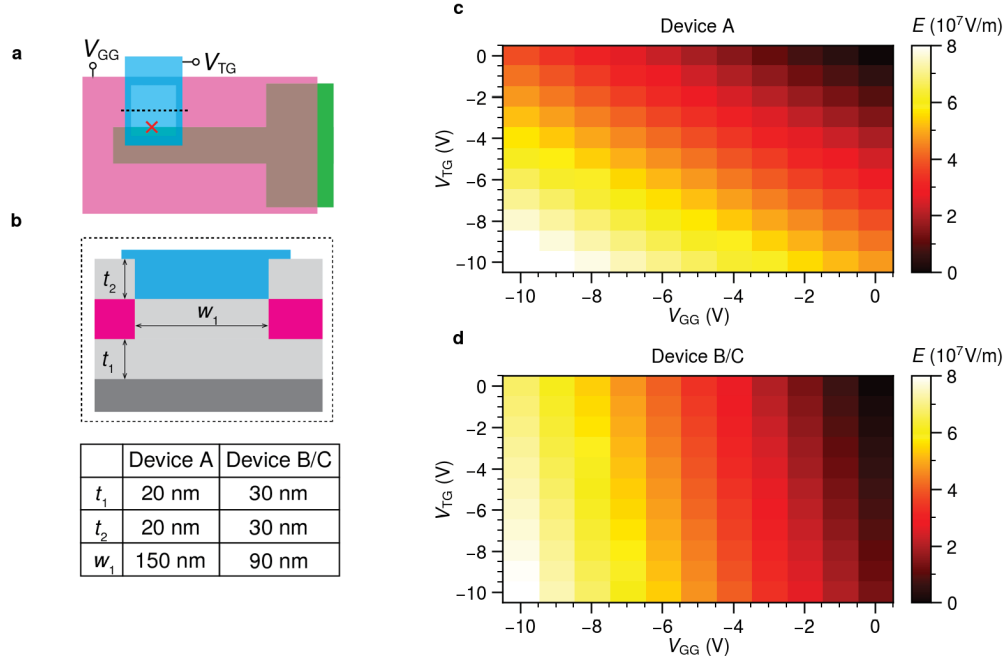


FIG. S5. **COMSOL simulations of devices.** (a) Top view of the multiprobe device, with only one representative pinhole on the global gate and only one tunnel gate. The simulated electric field strength at the red cross is chosen to represent the effect of the applied global gate voltages V_{GG} and tunnel gate voltages V_{TG} . (b) A cross-sectional view of the device stack, taken along the dashed line in (a). The length scales that are relevant for the electrostatics are the thickness of the first ALD layer (t_1), the thickness of the second ALD layer (t_2) and the width of the pinhole (w_1). The table summarizes these parameters. (c) The simulated electric field norm for device A as a function of V_{GG} and V_{TG} . The change in the field amplitude as a function of only TG or GG of the same range is very similar. (d) The simulated electric field norm for device B/C. In contrast to (c), now the global gate has a much stronger effect on the 2DEGs than the tunnel gate. This is consistent with the overall thicker dielectric thickness ($t_1 + t_2$) and the smaller pinhole width (w_1) in device B/C, compared to device A. This may explain the weaker tunnel gate effect on the measured spectrum Fig. S4, and the relatively stronger gating effect in device A Fig. S3. More details about the COMSOL simulation can be found in the methods section.

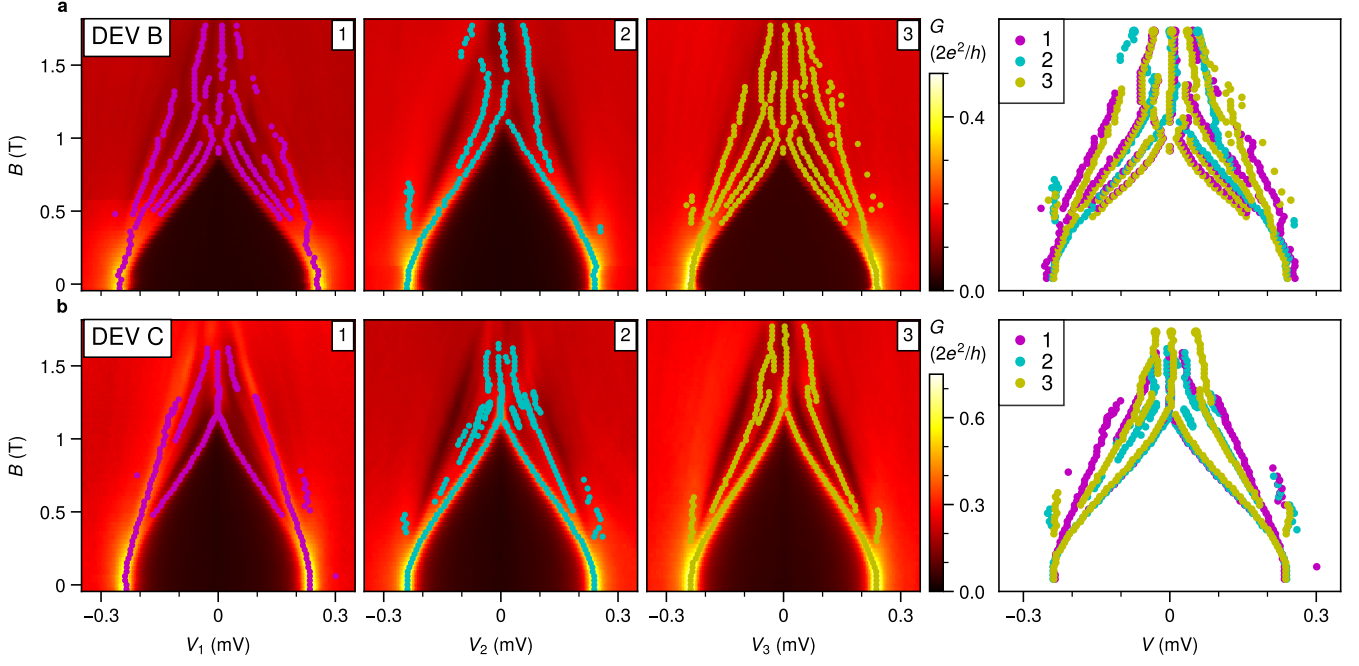


FIG. S6. **Identification of subgap states in Figure. 5: Device B and C.** At each field value, we find the local maxima in the tunnelling conductance and overlay these states from different probes in the last plot of each row. For device B ((a), top row), the lowest subgap states of probe 1 and probe 3 show identical dependence on magnetic field, but are absent in the spectra in probe 2. However, the evolution of the second-lowest states of probe 1 and 3 matches well with that of the lowest states of probe 2. For device C ((b), bottom row), the lowest energy subgap states from the three probes show identical dependence.

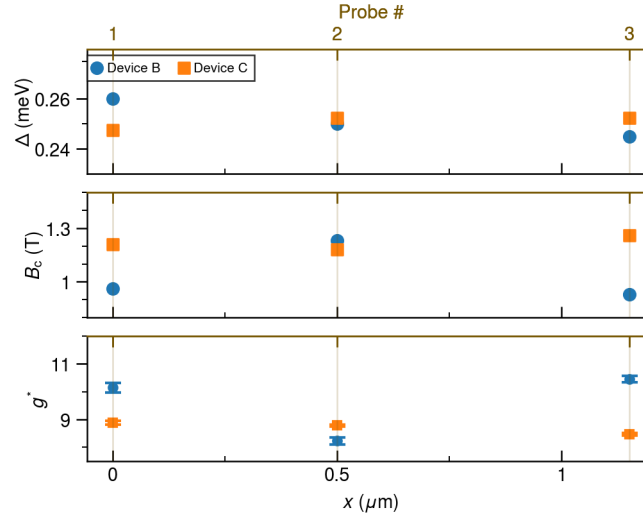


FIG. S7. **Spatial dependence of superconducting gap Δ , critical field B_c and effective g-factor g^* of the lowest subgap states: Device B and C.** For device B, the value of B_c and g^* at probe 2 is clearly different from those at probe 1 and 3. For Device C, however, these parameters are nearly identical at various probes.

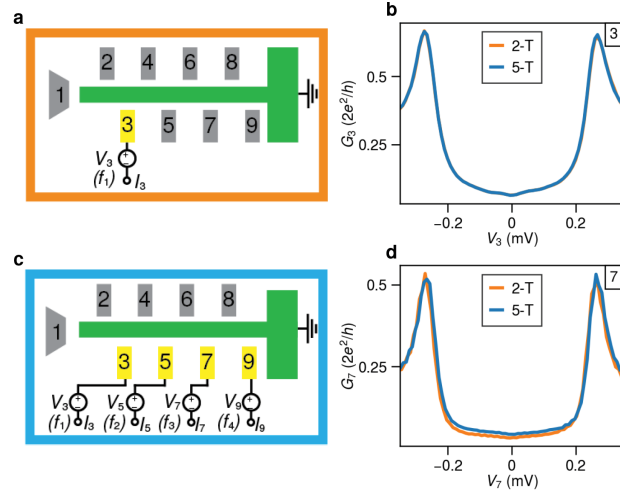


FIG. S8. **Comparison of the measured signal with different circuit configurations.** Measurements here are performed either with a two-terminal circuit diagram (with the voltage bias applied to either the probe 3, as shown in (a) or the probe 7) or a five-terminal circuit (with voltage biases applied simultaneously to four probes, shown in (c)). The measured conductance via two kinds of circuits are then plotted together for probe 3 (b) and probe 7 (d). There is no significant difference regarding the positions and heights of the coherence peaks between these two measurements, confirming the validity of the five-terminal circuit configuration for investigating the subgap states.